

# Application of laser ablation inductively coupled plasma (dynamic reaction cell) mass spectrometry for depth profiling analysis of high-tech industrial materials

Lieve I. L. Balcaen,<sup>a</sup> Jens Lenaerts,<sup>b</sup> Luc Moens<sup>a</sup> and Frank Vanhaecke<sup>\*a</sup>

<sup>a</sup> *Laboratory of Analytical Chemistry, Ghent University, Institute for Nuclear Sciences, Proeftuinstraat 86, B-9000 Ghent, Belgium. E-mail: Frank.Vanhaecke@UGent.be;*

*Fax: +32-(0)9-264.66.99*

<sup>b</sup> *Agfa-Gevaert N.V., Septestraat 27, B-2640 Mortsel, Belgium*

*Received 9th August 2004, Accepted 15th February 2005*

*First published as an Advance Article on the web 10th March 2005*

A 193 nm ArF excimer-based laser ablation system coupled to an inductively coupled plasma mass spectrometer equipped with a dynamic reaction cell (LA-ICP-DRC-MS) was successfully used for the depth profiling analysis of several (multi-layered) industrial materials characterised by markedly different ablation behaviours and sample composition. To obtain the optimum depth resolution for each of the samples, crater geometry and parameters such as laser pulse energy were studied as a function of the sample composition and layer thickness. Layers with a thickness of  $<1\ \mu\text{m}$  up to  $>200\ \mu\text{m}$  could be studied. Combining LA-ICP-MS data with results obtained by scanning electron microscopy (SEM) and profilometry allowed useful information about the crater geometry and the ablation depth per pulse to be obtained. In this way, it was possible to convert the original intensity-*versus*-time into intensity-*versus*-depth profiles and to evaluate the figures of merit of LA-ICP-MS for depth profiling studies. To illustrate the possibilities of the technique under investigation, depth profiling analysis of a thermographic material, a CsBr phosphor screen and thermal printing plates was carried out. In all cases, the spatial resolution of the laser ablation system was sufficient to differentiate between the separate layers (even for very thin layers of  $\pm 1\ \mu\text{m}$ ), which makes the technique suitable for studying trace element distributions and diffusion effects in several high-tech materials. Spectral interferences hampering the accurate determination of S and K in the printing plate were overcome by using chemical resolution in the DRC. The use of  $\text{O}_2$  as a reaction gas permitted the simultaneous determination of all elements of interest (S as  $\text{SO}^+$ , K as  $\text{K}^+$  and Zr as  $\text{ZrO}^+$ ).

## Introduction

Obtaining information on the spatial distribution of trace elements in high-tech industrial materials is of great importance. Whether the samples consist of a single layer or are multi-layered, and whether they are doped with specific elements to enhance their properties, or they are just contaminated with traces of different elements, it can be very useful to obtain information about the lateral distribution of some target elements and to identify concentration gradients as a function of depth (by means of depth profiling analysis). Therefore, an analysis technique with a good lateral and depth resolution is required.

For many years, spatially resolved and depth profiling analysis has been performed using various microanalytical techniques in which photons, electrons or ions interact with the sample surface. SIMS,<sup>1–2</sup> AES,<sup>3</sup> LIBS<sup>4</sup> and GD-OES<sup>5</sup> are a few of the techniques that are frequently used in this context. Although most of these methods are characterised by a depth resolution in the nm range, the poor lateral resolution, the necessity of matrix-dependent corrections and/or the low sample throughput make them less appropriate for various practical applications.

During the last five years, laser ablation inductively coupled plasma mass spectrometry (LA-ICP-MS) has been increasingly used for the direct analysis of a wide range of solid samples. This is mainly due to improvements in the laser systems, such as shorter wavelengths (higher energy), improved beam profile (flat-top), enhanced imaging systems and user-friendly software. In spite of these new developments, with most laser systems achieving ablation craters of the desired geometry

(flat-bottomed and straight-walled) and evaluating the information obtained by using LA-ICP-MS for depth profiling is still not self-evident. Ideally, every single laser pulse should remove a reproducible amount of sample from a layer of uniform depth and the relationship between the depth of the crater and the number of pulses should be linear. However, in practice, the exact rate of ablation depends on the material and several critical parameters can influence the geometry of the crater and the corresponding signals, *e.g.*, laser irradiance, laser type, the crater depth/diameter ratio and the occurrence of fractionation effects.<sup>6</sup> In this study, depth profiles have been investigated for various high-tech industrial materials consisting of layers of various thickness and ablation behaviour. Because of the great influence of the crater shape on the accuracy of the depth profiles, some of the craters obtained by using laser ablation were studied with scanning electron microscopy (SEM) and profilometry. In this way, information about the crater geometry and the rate of ablation can be combined with data available from ICP-MS measurements, leading to a better characterisation of the samples and a more profound insight into the processes taking place.

## Experimental

### Instrumentation

All ICP-MS measurements were carried out using a Perkin-Elmer SCIEX DRCplus quadrupole-based ICP-mass spectrometer (ON, Canada). This instrument is equipped with a dynamic reaction cell (DRC), which allows spectral interferences to be dealt with by means of chemical resolution. For this

purpose, highly pure reaction gases can be introduced into the DRC at controlled gas flow rates. In this work, ultrapure O<sub>2</sub> (>99.9995% purity, Air Liquide, Belgium) was used as a reaction gas for the determination of S and K. The O<sub>2</sub> gas flow rate mentioned in this paper is expressed in Ar-equivalent mL min<sup>-1</sup> (as read from the mass flow controller). To convert this into the actual O<sub>2</sub> gas flow rate, this value has to be multiplied by a factor of 0.70. This instrument is described in more detail by Baranov *et al.*<sup>7</sup>

Depth profiling analysis of the samples was accomplished by using a GeoLas 200M 193 nm ArF excimer-based laser ablation (LA) system for sample introduction (MicroLas, Germany). The original UV laser beam coming from the Compex 102 laser unit (LambdaPhysik, Germany) is transformed into a homogeneous beam with a high energy density (2–20 J cm<sup>-1</sup>) in an optical system, equipped with prisms, a homogeniser and appropriate lenses.<sup>8</sup> Crater diameters can be varied between 4 and 120 µm. In this application, the largest crater diameter was used to maximise the analyte signal intensities, except for the study of the Eu-distribution in CsBr, where the material was turned on its side and a line scan was performed with a laser beam of the smallest diameter attainable (4 µm). The ablation cell was coupled to the ICP torch by means of Tygon tubing (3 mm internal diameter). Ar was used as the carrier gas.

The most important ICP-MS and LA instrument settings and data acquisition parameters used throughout this work are summarised in Table 1.

To evaluate the geometry of the craters, a Jeol JSM-5600 SEM apparatus and a Dektak-8 stylus profiler were used.

## Samples

All samples—a thermographic material, printing plates and CsBr:Eu phosphor screens—were obtained from Agfa-Gevaert N.V. (Mortsel, Belgium), except for the SiC, which was provided by Umicore (Diepenbeek, Belgium).

The thermographic material consists of three major layers: a Si-containing polymer covering layer (1 µm thickness), an organic silver salt-based layer (the thermographic active layer—10 µm thickness) and a polymer (PET) support layer (175 µm thickness). This material is used as an alternative to more traditional products for printing medical radiographic images. Digital images can be printed with it by using a thermal printer. The different grey values, specific contrast and sensitivity are achieved by changing the heat energy transferred to the material by this printer. However, the presence and the spatial distribution of several elements can affect the properties of the material and the lifetime of the printer (*e.g.*, corrosion of the printer head). Therefore, the concentration and distribution of these elements should be checked during the manufacturing process.

LA-ICP-MS was also used to study analyte element distributions in printing plates. The plates analysed in this work consist of an aluminium substrate which is electrochemically roughened and covered with a surface layer of anodic aluminium oxide. Prior to application of a sensitive coating material, the substrate was subjected to a surface treatment (a post-anodic dip).<sup>9</sup> In this work, both the distribution of the contrast dye (copper phthalocyanine) in the active layer (sensitive coating) and of S, K and Zr in the treated aluminium substrate were studied to reveal the influence of the manufacturing conditions on the composition of the final product.

The phosphor screens are used in computed radiography and the latent image stored in the storage phosphor is read out by means of photostimulated luminescence. The screens contain a coating of photostimulable storage phosphors (CsBr:Eu or (Ba,Sr)(F,Br,I):Eu) that store energy upon X-ray exposure. A plate containing the storage phosphor is exposed in a light-tight cassette and then read out using a scanner to create the digital image.<sup>10</sup> These phosphor screens are known to be

**Table 1** Instrument settings and data acquisition parameters used for LA-ICP-MS analysis of industrial materials

<b>PerkinElmer Sciex DRCplus ICP-mass spectrometer</b>	
<i>Instrument settings</i>	
Rf power	1200 W
Gas flow rates:	
Plasma	17 L min <sup>-1</sup>
Auxiliary	1.2 L min <sup>-1</sup>
Nebuliser	1.4 L min <sup>-1</sup>
Sampling cone	Pt, 1.1 mm aperture diameter
Skimmer	Pt, 0.9 mm aperture diameter
Lens voltage	Optimised for maximum analyte signal intensity
<i>DRC mode (only for S and K determination)</i>	
Reaction gas and flow rate	O <sub>2</sub> , 0.4 Ar-equivalent mL min <sup>-1</sup>
RPq-setting	0.4
RPa-setting	0
Axial field potential	+200 V
<i>Data acquisition parameters</i>	
Scanning mode	Peak hopping
Dwell time per acquisition point	20–30 ms (depending on the application)
Number of acquisition points per spectral peak	1
Number of sweeps per reading	1
Number of readings per replicate	1
Number of replicates	Depending on the application and the time needed for ablation
<b>GeoLas laser ablation system</b>	
<i>Thermographic material</i>	
Laser pulse energy	100 mJ
Repetition rate	3 Hz
Crater diameter	120 µm
<i>Thermal printing plates</i>	
Laser pulse energy	12 mJ (Cu in active layer) 200 mJ (K, S and Zr in Al-substrate)
Repetition rate	1 Hz
Crater diameter	120 µm
<i>CsBr phosphor screens</i>	
Depth profiling analysis	
Laser pulse energy	40 mJ
Repetition rate	3 Hz
Crater diameter	120 µm
Line scan over the sample border	
Laser pulse energy	100 mJ
Repetition rate	20 Hz
Crater diameter	4 µm
Step distance	5 µm

advantageous over conventional X-ray film, due to their higher sensitivity, their fast read out times and their reusability. Because Cs halides are rather new in the field, but have gained great importance for X-ray imaging in recent years, more insight into the behaviour of these products is required.<sup>11</sup> The study of the Eu-distribution over the surface and in depth can lead to a better understanding of the processes that take place during image formation.

SiC is used in advanced semiconductor electronic device applications. SiC-based electronics and sensors can operate in hostile environments where conventional silicon-based electronics cannot function.<sup>12</sup> Although no specific trace elements were determined in this material, the sample was useful in the context of this work because of its extremely flat sample surface. With a surface roughness of <1 nm, the sample was perfectly suited for a study of the geometry of the craters produced by the 193 nm laser ablation system.

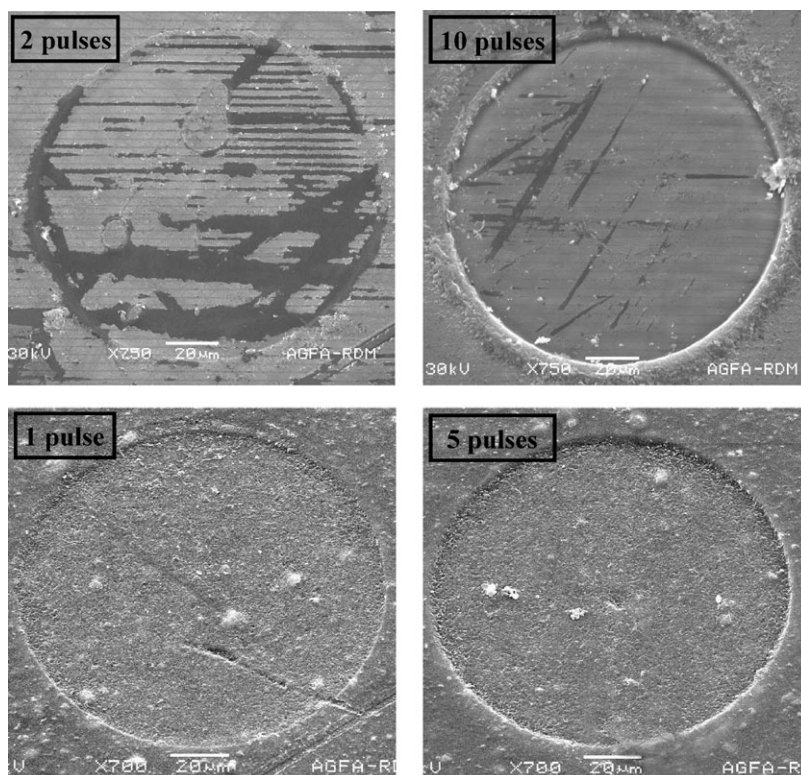


**Fig. 1** SEM pictures of craters obtained on ablation of (top) a SiC sample and (bottom) a thermographic material with a 193 nm ArF excimer-based laser ablation system.

## Results and discussion

### Depth profiling of multi-layered materials with well-defined layers

**Thermographic material.** To study the possibilities of laser ablation ICP-MS as a tool for depth profiling analysis of samples with well-defined layers, the thermographic material was selected because this sample consists of different layers of known thickness with a different (and specific) elemental composition. The covering layer (1  $\mu\text{m}$  thickness) contains Si compounds, while Ag is present (as an organic Ag salt) in the middle layer (10  $\mu\text{m}$  thickness) and the polymer (PET) support layer (175  $\mu\text{m}$  thickness) contains 150  $\mu\text{g g}^{-1}$  of Sb. Clear differentiation between the layers is strongly dependent on the amount of material removed per pulse and the crater geometry.

To study the shape of the craters obtained with our laser setup, a SiC-sample was initially used because of the flatness of the sample surface. The SEM images in Fig. 1 (top) show that the 193 nm laser system produces laser pulses with a uniform energy density, which result in flat-bottomed and straight-walled craters, an important prerequisite for accurate depth profiling. The lines visible on the sample are not defects in the sample itself, but scratches in the fine gold layer that was deposited on the sample as required for SEM analysis.

From the profilometry results for the SiC-sample in Table 2, it can be concluded that the crater depth varies more or less linearly with the number of pulses and that the amount of material removed per pulse is rather limited ( $\pm 100$  nm per pulse).

However, the crater shape and the ablation depth are not only controlled by the laser setup, but also by the composition of the material. Therefore, the thermographic material—a sample with a totally different composition and ablation behaviour from SiC—was also subjected to laser ablation analysis and the corresponding craters are shown in Fig. 1 (bottom). As can be seen, also for this material, the craters are flat-bottomed and straight-walled. No profilometry measure-

ments were carried out for the thermographic sample because the ablation rate can be easily derived from the LA-ICP-MS data reported in Fig. 2. The high spatial resolution of laser ablation ICP-MS and the specific elemental composition of the layers makes it possible to clearly distinguish between the three layers.

Taking into account the thickness of the first two layers and the time needed for ablation through these layers, an average ablation rate of 200 nm per pulse was calculated for this material. This is an excellent value, showing that LA-ICP-MS is a useful technique, even for studying trace element distributions in very thin ( $\sim 1$   $\mu\text{m}$ ) layers.

For example, the depth profile obtained for Mg in the thermographic material is shown in Fig. 3A. It can be seen that the element is only present in the covering layer. To

**Table 2** Total crater depths and ablation depth per pulse as obtained by means of profilometry for samples of different composition and ablation behaviour, ablated under the conditions given in Table 1

Number of pulses	Crater depth/ $\mu\text{m}$		CsBr phosphor screen
	SiC	Al substrate	
1	0.1		
2	0.2		
3	0.3		
5	0.4		
10	0.9	0.6	
15		0.8	
20		1.0	
40		1.9	
50	5.4		
200			52
450			119
Average ablation depth per pulse	100 nm per pulse	50 nm per pulse	260 nm per pulse



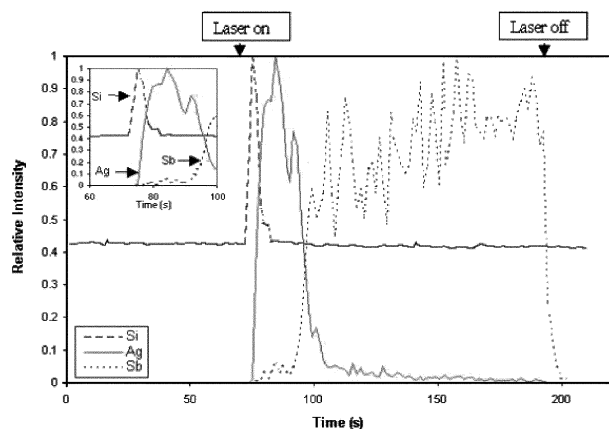


**Fig. 2** Results of depth profiling analysis of a thermographic material with a 193 nm ArF excimer-based laser ablation system. A laser pulse energy of 100 mJ, a repetition rate of 3 Hz and a crater size of 120  $\mu\text{m}$  were used. The intensities were normalised to the highest value obtained, in order to keep all the signals on the same scale.

confirm this, similar experiments were performed for a thermographic material without covering layer and as can be seen from Fig. 3B, the signal for Mg is at background level.

**Thermal printing plates.** As stated above, for the thermographic material, most elements could be assigned to one specific layer and almost no diffusion effects between the layers could be established. For several other materials, however, it is known that the active components, which are added to one layer, diffuse through the sample. This can change the characteristics of the materials drastically. As an example, thermal printing plates were studied.

The quality of these plates is, of course, dependent on the composition of the sensitive layer, but also the substrate and the post-anodic dip layer on top of it play an important role in the printing process. Because the manufacturing process seems to have a strong influence on the diffusion effects for the active layer, this layer was deposited on the substrate under four different conditions and all the samples were subjected to LA-ICP-MS analysis. All experiments were performed with a repetition rate of 1 Hz, a crater diameter of 120  $\mu\text{m}$  and a low laser pulse energy of 12 mJ. The Cu-profiles of two of the samples are shown in Fig. 4. While for condition 1 (not shown) and 2 (Fig. 4A) the Cu-signal was rather broad and extended into the Al substrate layer, the Cu diffusion could be more effectively avoided under conditions 3 (Fig. 4B) and 4 (not shown), as demonstrated by the narrower peaks and higher Cu concentrations at the sample surface. For comparison, similar experiments were performed with TOF-SIMS (Fig. 4C,D) and both methods provided similar information, namely that the Cu-distribution over the layer really depended on the conditions under which the active layer was deposited on the substrate. Although the depth resolution of TOF-SIMS is better than that of LA-ICP-MS, it should be mentioned that the analysis time is strongly reduced when using laser ablation-ICP-MS. Furthermore, most sample types can be handled with LA-ICP-MS, while TOF-SIMS is not as suited for the analysis of non-conducting samples (because of charging of the sample surface).

The study of the composition of the substrate (a roughened and partially anodised Al-layer) and the diffusion of components from the post-anodic dip layer ( $\text{K}_2\text{ZrF}_6$ ) is more complex because the porous  $\text{Al}_2\text{O}_3$  and the Al-layer have different ablation behaviours. Laser irradiance and the composition of the sample are two of the most important parameters that control the ablation efficiency and the depth resolution. On one

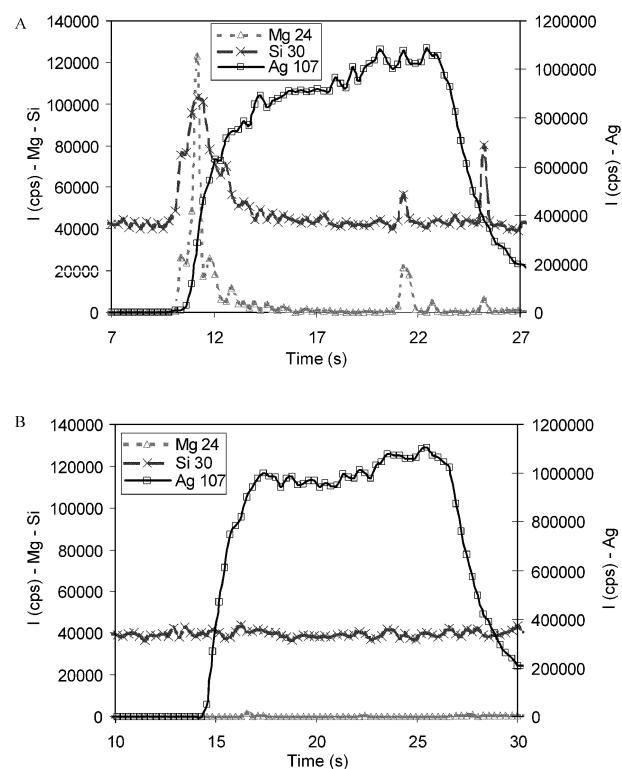


**Fig. 3** Results of depth profiling analysis of a thermographic material with, A, and without, B, covering layer. Results are shown for  $^{24}\text{Mg}$ . A laser pulse energy of 100 mJ, a repetition rate of 3 Hz and a crater size of 120  $\mu\text{m}$  were used.

hand, the laser irradiance should be sufficiently high to ablate the material efficiently and to maintain a uniform crater geometry at depth. On the other hand, an increased irradiance has a strong influence on the amount of material removed per pulse. As a compromise, Mason and Mank<sup>13</sup> suggested that the irradiance be set at a level 3–10 times higher than the ablation threshold for the sample material. However, if the sample consists of various layers with markedly different ablation behaviours, the laser energy should not only be suitable for the top layer, but also for the underlying layers. If the lower layer has a higher ablation threshold than the upper layer, it is possible that the lower layer cannot be efficiently ablated under the conditions optimised for the sample surface. Thus, the ablation behaviour has to be studied for each layer separately and a compromise must be reached.

For this application, both the  $\text{Al}_2\text{O}_3$  and the Al-layer were ablated with different laser energies and the corresponding Al signal intensities were studied. It was clear that the ratio of the Al signal intensity obtained for the Al-layer to that obtained for the  $\text{Al}_2\text{O}_3$ -layer was much lower when using an energy of 50 mJ than when using a 200 mJ energy. This indicates most probably an inefficient ablation of the Al-layer with a lower laser energy (which can be explained by the high reflectivity of Al). To be sure that the laser energy was high enough for obtaining an efficient ablation of both layers, all measurements were performed with a laser energy of 200 mJ. The drawback of using such high energy is that more material is removed per pulse, which reduces the maximum depth resolution that can be obtained.

Fig. 5A shows signal profiles obtained for a  $\text{K}_2\text{ZrF}_6$ -coated substrate. As can be seen, there is a clear offset in the Al-signal after 15–20 s of ablation which can be attributed to the transition between the  $\text{Al}_2\text{O}_3$ - and the Al-layer. Although one would expect, on the basis of the layer composition and density, that the Al signal intensity would be lower for the  $\text{Al}_2\text{O}_3$ -layer than for the Al-layer, it was observed that it was exactly the other way around. This can also be explained by the

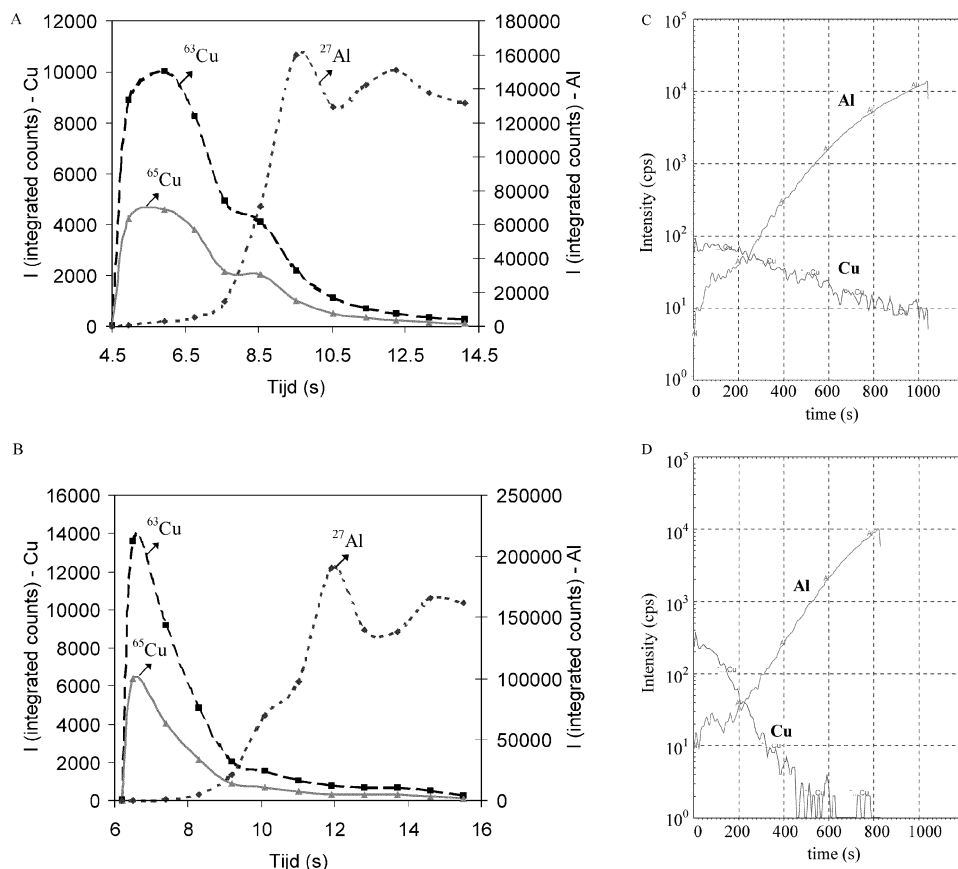


**Fig. 4** Study of the Cu distribution in the active layer of a thermal printing plate as a function of the manufacturing conditions with a 193 nm ArF excimer-based laser ablation system (A: condition 2; B: condition 3). A laser pulse energy of 12 mJ, a repetition rate of 1 Hz and a crater size of 120  $\mu\text{m}$  were used. For comparison, analogous experiments were performed with TOF-SIMS (C: condition 2; D: condition 3).

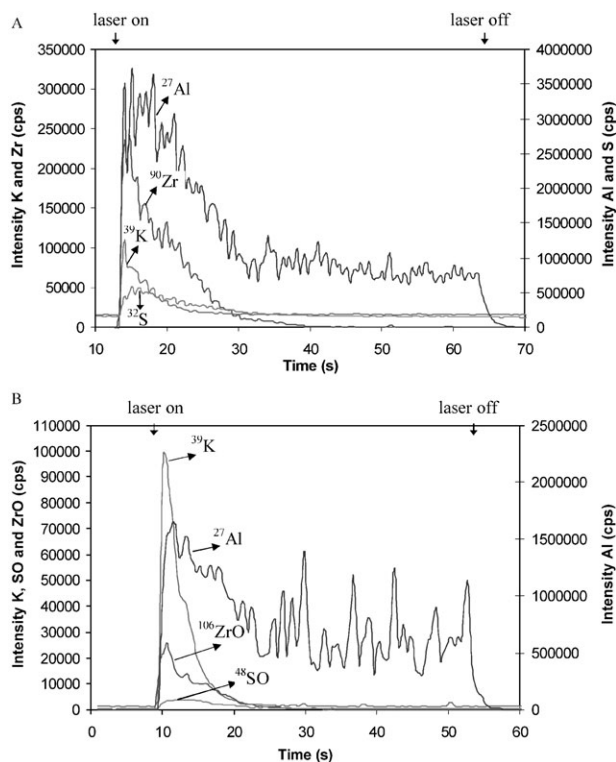


**Fig. 5** Study of the distribution of S, K and Zr in a treated and partially anodised aluminium substrate for printing plates. A repetition rate of 1 Hz and a crater size of 120  $\mu\text{m}$  were used. Both figures were obtained with a laser pulse energy of 200 mJ. Part B was obtained by using  $\text{O}_2$  as a reaction gas in the dynamic reaction cell to allow the interference-free detection of S as  $\text{SO}^+$ , K as  $\text{K}^+$  (and Zr as  $\text{ZrO}^+$ ).

higher reflectivity of the Al-layer compared with the  $\text{Al}_2\text{O}_3$ -layer.

At the level of the transition point, a clear decrease in the Zr-signal can be observed, indicating that the Zr ions are only present in the post-anodic-dip layer and the oxide layer, but not in the Al-layer. Although there is an enrichment of Zr at the surface of the sample, there is still an important fraction of the Zr present in the oxide-layer, so it can be concluded that the Zr ions have diffused through the entire  $\text{Al}_2\text{O}_3$ -layer.

With regard to the S-signals, it was observed that there was a markedly higher signal intensity during the ablation of the oxide layer. This could be expected because the anodising of the Al-layer was carried out in a  $\text{H}_2\text{SO}_4$  bath. K on the other hand was only expected in the post-anodic dip layer and the fact that the K-signal was spread over the oxide layer as well suggested that diffusion effects were taking place. However, one should be aware of the fact that the determination of S and K with a traditional quadrupole-based ICP mass spectrometer is not straightforward due to the occurrence of spectral overlap between the analyte signals and those of O- (e.g.,  $\text{O}_2^+$ ) and Ar-based (e.g.,  $^{38}\text{ArH}^+$  and  $^{38}\text{Ar}^+/\text{}^{40}\text{Ar}^+$  tailing) ions, respectively, as is illustrated by the high gas blanks. Fortunately, both problems can be tackled by using chemical resolution in a dynamic reaction cell.

The DRC approach traditionally used to deal with the spectral interferences hampering the accurate determination of  $\text{K}^+$  is the use of  $\text{NH}_3$  as a reaction gas.<sup>14</sup> The signal-to-background-ratio for K could be improved by a factor of  $\pm 20$  by using  $\text{NH}_3$  for the sample studied in this work. Unfortunately, the  $\text{S}^+$  and  $\text{Zr}^+$  ions also react with the  $\text{NH}_3$ , resulting in the formation of neutral  $\text{S}^{15}$  and  $\text{Zr}(\text{NH}_3)_x^+$ -complexes (as could be established by monitoring the signals at mass-to-charge ratios of 107, 124 and 141), respectively. Owing to these reactions, the simultaneous determination of S, K and Zr in

printing plates was impossible when using  $\text{NH}_3$  as a reaction gas. However, a systematic study of the literature for bimolecular gas phase cation-molecule reaction kinetics<sup>16</sup> revealed that  $\text{O}_2$  could be used as an alternative to  $\text{NH}_3$  for the interference-free or at least less-interfered determination of  $\text{K}^+$ . Indeed, while  $\text{K}^+$  shows no reactivity towards  $\text{O}_2$ ,<sup>17</sup> the reaction of the interfering  $\text{ArH}^+$  with  $\text{O}_2$  is thermodynamically allowed and fast.<sup>15</sup> Under optimised conditions, the signal-to-background-ratio for K could also be improved by a factor of 20 by using  $\text{O}_2$ . Although the improvement in signal-to-background-ratio that could be obtained was similar when using  $\text{NH}_3$  and  $\text{O}_2$ , the latter approach was preferred because the simultaneous determination of S and Zr was enabled by using  $\text{O}_2$  as a reaction gas. Bandura *et al.*<sup>18</sup> developed a method that uses reaction with  $\text{O}_2$  in a dynamic reaction cell to oxidise  $\text{S}^+$  and to allow its interference-free or at least less-interfered detection as  $\text{SO}^+$ . To reduce the collisional scattering of the parent and product ions with the relatively heavy reaction gas (and enhance the sensitivity in this way), a d.c. axial field was introduced to “herd” the ions through the reaction cell. Under optimised conditions, the signal-to-background-ratio could be improved by a factor of 4 by measuring  $^{48}\text{SO}^+$  in DRC mode instead of  $^{32}\text{S}^+$  in standard mode.

With regard to the Zr, it was observed that the signal intensity dropped tremendously in the presence of oxygen. This corresponds with the findings of Eiden *et al.*,<sup>19</sup> who showed that the signal of  $\text{Zr}^+$  is suppressed by oxidation with  $\text{O}_2$ . Calculation of  $\Delta H_r$  for the O-atom transfer reaction<sup>20</sup> confirms that the reaction is thermochemically favourable in this instance and that Zr can be measured as  $\text{ZrO}^+$ .

The reaction gas flow rate and other instrumental parameters used in this part of the work are summarised in Table 1.

The signal profiles in Fig. 5B were recorded under optimised DRC-conditions. Comparison with Fig. 5A confirms the conclusions drawn before, namely that S, K and Zr are all spread over the entire  $\text{Al}_2\text{O}_3$ -layer, although K and Zr are partially enriched at the surface. The accuracy of these results could be confirmed by comparison with similar experiments performed by means of TOF-SIMS.

### Depth profiling studies for thick ( $>200\ \mu\text{m}$ ) layers or layers of an inhomogeneous thickness

While depth profiling studies by means of LA-ICP-MS seem to provide accurate information about the analyte distribution and concentration gradients for well-defined, thin layers, the situation becomes more complex when the sample consists of thicker layers or layers of inhomogeneous thickness. On the one hand, the original data produced by means of LA-ICP-MS are intensity-*versus*-time diagrams and the ablation depth per pulse (or per time unit) is dependent on the sample composition. To illustrate this fact, craters in different materials (SiC, anodised Al substrate and CsBr phosphor screens) were studied by means of profilometry. From Table 2, it can be seen that for each of these materials, the depth varies more or less linearly with the number of laser pulses. However, there is an important difference in the average ablation depth per pulse between the different samples which makes it nearly impossible to convert intensity-*versus*-time diagrams directly into intensity-*versus*-depth diagrams. On the other hand, it is known that for the LA-system used in this work, the crater depth to crater diameter ratio should be  $<1.5$  to obtain accurate depth profiles.<sup>6</sup>

In this context, the Eu-distribution in CsBr phosphor screens was studied. Because of the large thickness of the sample ( $\pm 500\ \mu\text{m}$ ) and the specific characteristics of LA-ICP-MS (as discussed above), ablating through the entire layer from one side of the sample (from the top to the bottom) could give rise to erroneous results. Therefore, measurements were performed from the top to the middle on the one hand (Fig. 6A) and from the bottom to the middle on the other hand (Fig. 6B). A disadvantage of this method is that no real depth information can be obtained and that it is difficult to figure out at which point both graphs overlap. However, studying the corresponding craters by means of profilometry can partially solve the problem. In Fig. 6C and 6D the results from both the LA-ICP-MS (Fig. 6A,B) and the profilometry (Table 2) experiments are combined, and it can be concluded that the Eu enrichment at the top is spread out over a distance of  $\pm 120\ \mu\text{m}$ , while the peak at the bottom is smaller and only spread out over a

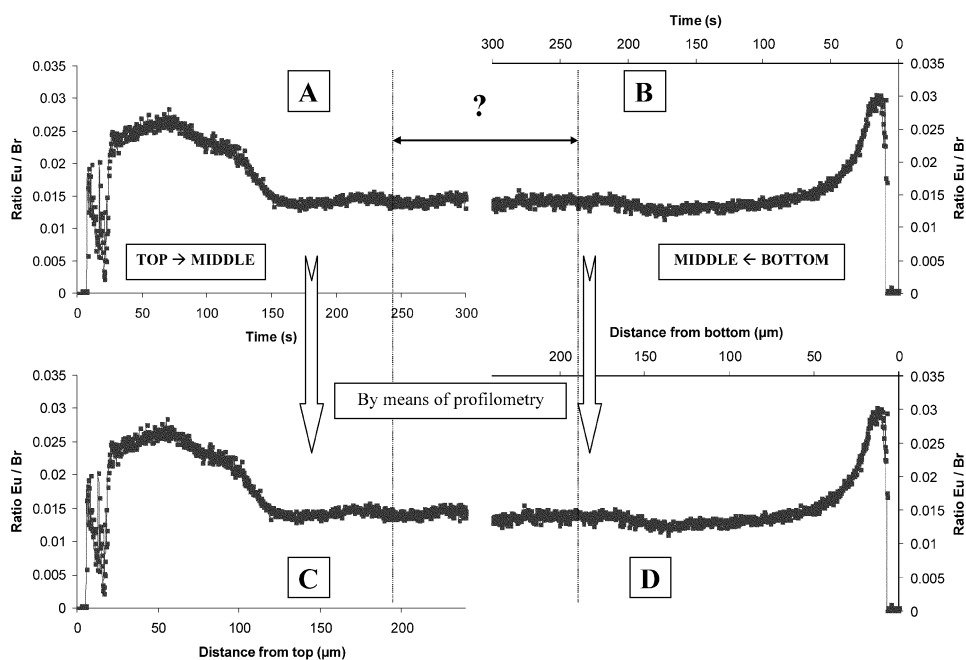


**Fig. 6** Study of the distribution of Eu in CsBr phosphor screens. A laser pulse energy of 40 mJ, a repetition rate of 3 Hz and a crater size of 120  $\mu\text{m}$  were used. Because of the layer thickness, the sample was ablated (A) from the top to the middle and (B) from the bottom to the middle. To convert both graphs into their corresponding intensity-*versus*-depth profiles (C and D, respectively), the ablation depth per pulse was determined by means of profilometry.



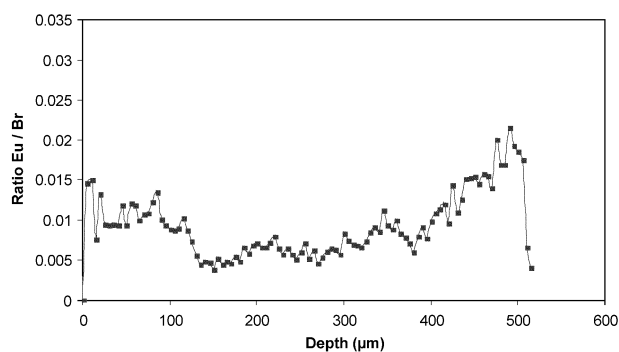


**Fig. 7** The CsBr:Eu sample from Fig. 6 was turned on its side and a line scan was performed over the sample edge with a laser energy of 100 mJ, a repetition rate of 20 Hz, the smallest crater diameter available (4  $\mu\text{m}$ ) and a step distance of 5  $\mu\text{m}$ .

distance of  $\pm 50 \mu\text{m}$ . The enrichments at the sample surfaces are the result of the way in which these CsBr layers are manufactured. It should be mentioned that in all graphs the ratio of Eu to Br was reported instead of the Eu-signal itself. Indeed, it is known that as craters become deeper, the overall response for homogeneously distributed elements decreases, reflecting the reduced extraction efficiency of the gas flushed across the sample.<sup>6</sup> This problem can be corrected by dividing the intensity of the analyte element with that of a matrix element, assuming that fractionation effects are negligible. Furthermore it should be noticed that a covering layer was present on top of the CsBr samples, which explains the delay in the enhancement of the Eu/Br signal in Fig. 6A and 6C. After removal of the surface contamination by means of ablation, the signal first decreases during sampling of the covering layer, and rises again as soon as the CsBr layer is reached.

To check the accuracy of these results, the same sample (but without a covering layer) was also turned on its side and a line scan was performed over the sample edge with a laser beam of the smallest diameter attainable (4  $\mu\text{m}$ ). The laser was fired 20 times at a frequency of 20 Hz at each spot. The step distance (the distance moved by the sample stage between two spots) was set at 5  $\mu\text{m}$  to give adjacent but non-overlapping craters. To obtain intensity-versus-depth profiles, the intensity for each crater was plotted as a function of the distance in the sample and the resulting depth profile is shown in Fig. 7. Comparison with the results from Fig. 6 shows that both methods provide similar information, namely that the Eu concentration is enhanced in the first 120  $\mu\text{m}$  and the last 50  $\mu\text{m}$ , with a more or less 'flat' signal in between. However, it can be noticed that the second peak in Fig. 7 is somewhat broader than the one in Fig. 6. This imperfect agreement can be explained by the different orientation of the CsBr needles with respect to the laser beam (lateral instead of head-on ablation). Moreover, the diameter of the laser beam used for performing the line scan over the sample edge is similar to the diameter of the CsBr

needles, so that only one needle is sampled. For the head-on ablation, on the other hand, a laser beam of 120  $\mu\text{m}$  diameter is used, and many needles are sampled at the same time (Fig. 8).

Which of the two methods is to be preferred depends on the information required and the expectations in terms of sample throughput. The signals obtained by means of depth profiling (drilling) at a fixed point are detailed (one data point every 0.3  $\mu\text{m}$ ) and sensitive (due to the use of the largest crater diameter attainable) and the sample throughput is very high. On the other hand, interpretation of the data obtained for thicker layers is not straightforward and additional information, e.g., based on results of profilometry studies, is required to convert the signal-versus-time profiles into signal-versus-depth profiles. By turning the sample on its side and performing a line scan over the sample edge signal-versus-depth profiles can be obtained even for very thick layers, making interpretation of the data much easier. A few drawbacks of this method are the longer analysis time, the less detailed depth profiles (only one data point every 5  $\mu\text{m}$ ) and the loss in sensitivity due to the use of smaller crater diameters (4  $\mu\text{m}$ ). Furthermore, it is technically more difficult to achieve a laser spot with such a small diameter.

## Acknowledgements

Lieve Balcaen is a Research Assistant of the Fund for Scientific Research–Flanders (FWO-Vlaanderen), which is also acknowledged for financial support (research project G.0037.01). The authors are grateful to Gina De Lamper, Peter Van Rompuy and Monique Moens for their help with the SEM, profilometry and TOF-SIMS measurements, respectively. Geert Seghers (Umicore) is acknowledged for providing the SiC disc.

## References

- 1 T. Kolber, K. Piplits, L. Palmethofer and H. Hutter, *Microchim. Acta*, 2000, **135**, 105–111.
- 2 P. C. Zalm, *Microchim. Acta*, 2000, **132**, 243–257.
- 3 M. Prutton, D. K. Wilkinson and D. A. Loveday, *Microchim. Acta*, 2000, **132**, 225–236.
- 4 J. M. Vadillo and J. J. Laserna, *J. Anal. At. Spectrom.*, 1997, **12**, 859–862.
- 5 F. Präzler, V. Hoffmann, J. Schumann and K. Wetzig, *J. Anal. At. Spectrom.*, 1995, **10**, 677–680.
- 6 P. R. D. Mason and A. J. G. Mank, in *Laser-ablation-ICPMS in the earth sciences: principles and applications*, ed. P. Sylvester, Short Course Series Volume 29, Mineralogical Association of Canada, Ottawa, 2001, p. 93.
- 7 V. I. Baranov and S. D. Tanner, *J. Anal. At. Spectrom.*, 1999, **14**, 1133–1142.
- 8 D. Günther, *J. Anal. At. Spectrom.*, 1997, **12**, 939–944.
- 9 F. R. Mayers and T. V. Chau, *Production of support for lithographic printing plate*, 2004-04-23 ([www.uspto.gov/patft/index.html](http://www.uspto.gov/patft/index.html)).
- 10 P. J. R. Leblans, *New needle-crystalline detector for X-ray computer radiography*, 2004-04-23 ([www.ndt.net/article/ecndt02/44/44.htm](http://www.ndt.net/article/ecndt02/44/44.htm)).
- 11 P. Hackenschmied, G. Schierner, M. Batentschuk and A. Winnacker, *J. Appl. Phys.*, 2003, **93**, 5109–5112.
- 12 P. Neudeck, *Silicon Carbide High Temperature Integrated Electronics and Sensors*, 2004-04-23 ([www.grc.nasa.gov/WWW/SiC/SiC.html](http://www.grc.nasa.gov/WWW/SiC/SiC.html)).
- 13 P. R. D. Mason and A. J. G. Mank, *J. Anal. At. Spectrom.*, 2001, **16**, 1381–1388.
- 14 S. D. Tanner, V. I. Baranov and U. Vollkopf, *J. Anal. At. Spectrom.*, 2000, **15**, 1261–1269.
- 15 V. G. Anicich, *J. Phys. Chem. Ref. Data*, 1993, **22**, 1469.
- 16 V. G. Anicich, *JPL publication 03-19*, California Institute of Technology, Pasadena, November 2003.
- 17 R. Johnsen, H. L. Brown and M. A. Biondi, *J. Chem. Phys.*, 1971, **55**, 186–188.
- 18 D. R. Bandura, V. I. Baranov and S. D. Tanner, *Anal. Chem.*, 2002, **74**, 1497–1502.
- 19 G. C. Eiden, C. J. Barinaga and D. W. Koppenaal, *J. Anal. At. Spectrom.*, 1999, **14**, 1129–1132.
- 20 D. R. Bandura, V. I. Baranov and S. D. Tanner, *Fresenius' J. Anal. Chem.*, 2001, **370**, 454–470.

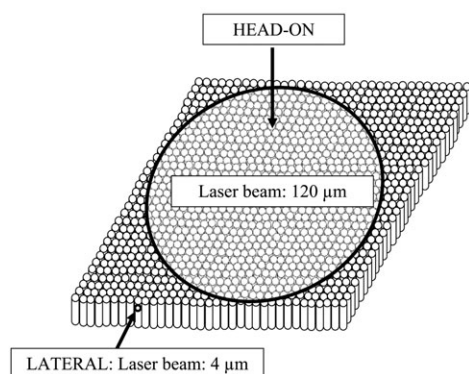


**Fig. 8** Difference between head-on and lateral ablation.